

University of Nevada, Reno

Variability in Pyroconvection During the Bootleg Fire in 2021

A thesis submitted in partial fulfillment of the requirements for the degree of Master of
Science in Atmospheric Science

by

Braeden Winters

Dr. Neil Lareau/Thesis Advisor

December 2024



THE GRADUATE SCHOOL

We recommend that the thesis
prepared under our supervision by

Braeden Winters

entitled

**Variability in Pyroconvection During the Bootleg Fire in
2021**

be accepted in partial fulfillment of the
requirements for the degree of

Master of Science

Neil Lareau
Advisor

Vera Samburova
Committee Member

Alexandra Lutz
Graduate School Representative

Markus Kemmelmeier, Ph.D., Dean
Graduate School

December, 2024

Abstract

We examine the factors controlling the depth and vigor of pyrocumulus (pyroCu) and pyrocumulonimbus (pyroCb) clouds during the Bootleg Fire in Oregon, USA (July 2021). A combination of Next Generation Weather Radar (NEXRAD) and Geostationary Operational Environmental Satellite number 17 (GOES-17) observations are used to characterize the wildfire's plume depth and the presence of pyroCu/Cb. These data are contextualized with High Resolution Rapid Refresh (HRRR) analysis fields to examine the thermodynamic structure of the atmosphere, and with GOES-17 Fire-Radiative Power (FRP) to characterize the fire's forcing for plume development. Results show a range of plume depths and pyroconvective outcomes, spanning dry convective columns with maximum depths <8 km, to deep pyroCb (~13 km MSL) with precipitation and lightning. We find that the plume height relative to the convective condensation level (CCL) discriminates between pyroCu and non-pyroCu periods. For pyroCb formation, we examine FRP relative to the PyroCb Firepower Threshold (PFT), which measures how much energy is needed to initiate moist convection. We find that the FRP's exceedance of the PFT adequately predicts pyroCb initiation, albeit not necessarily its longevity or spatial extent. We also explore the relationship between the plume rise geometry and pyroCb formation, finding that plume uprightness is associated with its ability to cross the CCL and form pyroCu/Cb. Lastly, we explore the terms Fire Convective Available Potential Energy (Fire CAPE) and Fire Convective Inhibition (Fire CIN) to describe the instability of the environment around the fire, providing insights into the fire's proclivity to initiate pyroCu/Cb. Ultimately our results will help forecasters identify when a fire is likely to produce pyroCb.

Contents

1. INTRODUCTION.....	ERROR! BOOKMARK NOT DEFINED.
2. BACKGROUND	3
3. DATA AND METHODS	7
3.1 THE BOOTLEG FIRE.....	7
3.2 ANALYSIS APPROACH	8
3.2.1 Model Data.....	9
3.2.2 Satellite Data.....	10
3.2.3 Radar Data	14
4. RESULTS	14
4.3 FIRE POWER THRESHOLD.....	24
4.4 PLUME GEOMETRY	28
4.4.1 10 July.....	30
4.4.2 14 July.....	32
5. DISCUSSION AND CONCLUSIONS	34

LIST OF TABLES

TABLE 1 FIRE CAPE, FIRE CIN, PFT, AND FRP_{x10} ON 15 JULY AT 02:00 UTC (CORRESPONDING WITH THE SKEW-T DIAGRAM DISPLAYED IN FIG. 9A) AND ON 19 JULY AT 00:00 UTC (CORRESPONDING WITH THE SKEW-T DIAGRAM DISPLAYED IN FIG. 9B).	28
TABLE 2 MAXIMUM FRP_{x10} FROM THE HOUR PRECEDING PYROCB INITIATION, PFT AT TIME OF INITIATION, AND F/U RATIO FOR THE 10 JULY PYROCB.....	30
TABLE 3 MAXIMUM FRP_{x10} FROM THE HOUR PRECEDING PYROCB INITIATION, PFT AT TIME OF INITIATION, AND F/U RATIO FOR THE 14 JULY PYROCB.....	32

LIST OF FIGURES

FIGURE 1 PYROCLOUD FORMING OVER THE BOOTLEG FIRE ON 16 JULY 2024. (PAYTON BRUNI/AFP/GETTY).....	1
FIGURE 2 SUMMARY OF THE BOOTLEG FIRE’S SPREAD BASED ON VIIRS HOT-SPOT DETECTIONS. THE COLOR OF THE MARKERS INDICATES THE DATE OF THE DETECTION AND THE SIZE OF THE MARKER THE RELATIVE FIRE INTENSITY (MEASURED IN TERMS OF THE FIRE-RADIATIVE POWER (FRP))......	8
FIGURE 3 (A) GOES “RED” VISIBLE IMAGERY WITH A PYROCb “PUFF” DETACHED FROM THE UPDRAFT AT 22:37 UTC ON 10 JULY, (B) GOES LONGWAVE IR, (C) RADAR CONTOURS AND PIXELS FLAGGED AS PYROCu (MAGENTA) BASED ON THE ADAPTIVE ALBEDO THRESHOLD, AND (D) RADAR CONTOURS AND PIXELS FLAGGED AS PYROCb (MAGENTA)......	11
FIGURE 4 (A) 3-D RECONSTRUCTION OF THE BOOTLEG FIRE’S SMOKE PLUME ON 14 JULY 2021 AT 23:30 UTC USING DATA FROM THE KMAX NEXRAD RADAR. GOES FRP PIXELS FROM THE FDC ON 14 JULY 2021 22:37 UTC. DISPLAYED PIXELS ARE (B) RAW DATA FROM GOES-17, AND (C) CORRECTED FOR SATURATION AND CLOUD-CONTAMINATION. SATURATED PIXELS ARE FILLED WITH 3,000 MW AND CLOUD-CONTAMINATED PIXELS ARE FILLED USING A REGRESSION ANALYSIS BETWEEN 3.9 μM BT’S AND FRP VALUES FOR NON-CLOUD-CONTAMINATED, NON-SATURATED PIXELS.	13
FIGURE 5 (A) MAXIMUM REFLECTIVITY (SHADED), CCL HEIGHT (BLACK LINE), LCL HEIGHT (DASHED BLACK LINE), -20°C TEMPERATURE HEIGHT (CYAN LINE) WHICH IS THE CLOUD TOP TEMPERATURE WHERE WE QUANTIFY PYROCb, AND THE HOMOGENEOUS FREEZING LEVEL (MAGENTA LINE). (B) NUMBER OF PIXELS DETECTED FROM GOES-17 FOR CUAMB (BLACK), PYROCu (BLUE), AND PYROCb (RED, MULTIPLIED BY 10). (C) LOWEST CLOUD-TOP TEMPERATURE, DIVIDED INTO NON-PYROCb TEMPERATURES (BLACK), PYROCb TEMPERATURES BASED ON THE -20°C THRESHOLD (BLUE), AND TEMPERATURES AT OR BELOW THE HOMOGENOUS FREEZING LEVEL (MAGENTA). (D) PFT (DARK RED) AND PFT _{APPROX} (DASHED RED) OVERLAID ON TOP OF THE FRP _{x10} (BLACK). (E) FIRE CAPE (RED) AND FIRE CIN (BLUE)......	15
FIGURE 6 DISTRIBUTIONS OF PLUME TOP HEIGHT MINUS THE CCL (ΔH) FOR (A) PYROCu AND (B) PYROCb.	18
FIGURE 7 FIRE CAPE (RED) AND FIRE CIN (BLUE) VALUES OVERLAID ON TOP OF THE MOST ACTIVE PYROCb PERIOD (SHADED YELLOW).	20
FIGURE 8 NUMBER OF PYROCb PIXELS DETECTED GIVEN VALUES FOR FIRE CAPE AND FIRE CIN (SHADED).	21
FIGURE 9 SKEW-T DIAGRAMS FROM (A) 02:00 UTC ON 15 JULY, AND (B) 00:00 UTC ON 19 JULY. THE SOLID RED AND BLUE LINES REPRESENT TEMPERATURE AND DEWPOINT,	

RESPECTIVELY, WHILE THE DASHED BLACK LINE REPRESENTS A CONVECTIVELY LIFTED PARCEL TEMPERATURE.....	23
FIGURE 10 THE DIFFERENCE BETWEEN FRP_{x10} AND PFT FOR (A) PYROCU AND (B) PYROCB.	25
FIGURE 11 THE DIFFERENCE BETWEEN FRP_{x10} AND PFTAPPROX FOR (A) PYROCU AND (B) PYROCB.	27
FIGURE 12 (A) PYROCB PULSE OVER THE BOOTLEG FIRE ON 10 JULY AT 22:17 UTC SEEN ON GOES-17 VISIBLE “RED” IMAGERY, AND (B) RADAR CROSS-SECTION WITH MAXIMUM RADAR REFLECTIVITY FROM 21:56 THROUGH 23:03 UTC ON 14 JULY WITH BRIGGS’ PLUME RISE CURVES OVERLAID, AND CORRESPONDING MIXED LAYER WINDS SPEEDS AND F/U RATIOS.	31
FIGURE 13 (A) PYROCB PULSE OVER THE BOOTLEG FIRE ON 14 JULY AT 23:32 UTC SEEN ON GOES-17 VISIBLE “RED” IMAGERY, AND (B) RADAR CROSS-SECTION WITH MAXIMUM RADAR REFLECTIVITY FROM 23:10 UTC ON 14 JULY THROUGH 00:12 UTC ON 15 JULY WITH BRIGGS’ PLUME RISE CURVES OVERLAID, AND CORRESPONDING MIXED LAYER WINDS SPEEDS AND F/U RATIOS.	33

1. Introduction



Figure 1 Pyrocloud forming over the Bootleg Fire on 16 July 2024. (Payton Bruni/AFP/Getty)

Increasing wildfire occurrence and intensity (Westerling et al., 2006; Dennison et al., 2014; Westerling, 2016; Wotten et al., 2017; Dowdy et al., 2019) associated with devastating societal impacts (Nauslar et al., 2018; Juliano et al., 2023, 2024) and far-reaching climatic effects (Peterson et al., 2018; Peterson et al., 2021; Liu et al., 2022) necessitates renewed focus on improving forecasts for extreme fire behavior. In particular, there is a need to better understand the processes contributing to “blow ups” in which fires experience rapid growth and intensification associated with a positive feedback loop amongst buoyant updrafts, moist-instability (i.e., fire-generated convective clouds), fire-generated inflow winds, and fire intensity. This feedback loop is often visually manifested

by the sudden growth of towering smoke plumes (Wilmot et al., 2022) capped with pyrocumulus (pyroCu) clouds, which may further develop into hazardous pyrocumulonimbus (pyroCb) clouds (Fig. 1) as they rise to the upper troposphere and glaciate (American Meteorological Society, 2021). The rapid vertical growth of these cloud-topped smoke columns is driven not only by the fire's heat, but also by the latent heating within the cloud, which reinvigorates the updraft (Trentmann et al., 2006) and is thought to sometimes feedback on surface fire behavior and intensity. For example, pyroCb initiation can introduce a new set of hazards in the fire-environment including lightning, which poses risks of additional lightning-ignited fires (e.g. Dowdy et al., 2017), precipitation causing downdrafts and outflows (Fromm et al. 2022), fire-generated tornadic vortices (FGTV's) (Fromm et al., 2006; Lareau et al. 2022), and long-range spotting. Accordingly, when pyroCb occur, direct aerial and ground-based attack on the fire is often not possible, allowing fires to continue to grow. For these reasons pyroCbs are considered a critical and dangerous form of fire weather.

In recognition of the threats posed by pyroCb, there are a number of emerging tools that attempt to forecast the transition to blow up conditions and the initiation of pyroCb. These include climatologically informed conceptual models (Peterson et al. 2017a), thermodynamic analysis of moist convective potential relative to fire heat input (Tory et al. 2021), and other thermodynamic-based analyses to estimate when plumes are likely to experience rapid vertical growth (Leach & Gibson, 2021). These approaches, however, remain mostly unvalidated in real-world fires. As such, the goal of this paper is to confront existing pyroCb forecast tools and concepts with process-level observations of a large wildland fire, the Bootleg Fire, that produced day-after-day pyroconvection of varying

depths, and thus provides an ideal testbed for isolating critical fire and environmental ingredients for pyroCb initiation and to test forecasting approaches. Specifically, we examine two questions:

1. How high do smoke columns need to rise before they condense to form pyroCu/Cb?
2. How much heating must be added by the fire to the lower atmosphere to initiate deep moist convection?

2. Background

While pyroCb development and “blow-ups” are not necessarily synonymous, it is useful to review traditional metrics for blow-up behavior on fires. Historically, lower-atmospheric stability indices, such as the Haines Index (HI; Haines, 1988), have been used to assess a fire’s blow up potential. The HI uses the dewpoint depression and lower-atmospheric lapse rates to determine fire risk, evaluated on a scale of 1-6. In general, larger HI values occur when the atmosphere is unstable with a steep lapse rate and dry near-surface conditions. For large HI values, it is expected that fires will become more “plume-dominated”, meaning upright convective columns and erratic fire-generated winds. In reality, the HI and its variants (e.g., continuous HI (Mills & McCaw, 2010)) have proven insufficient in fully distinguishing between extreme and gradual fire spread or isolated plume-dominated conditions (Winkler et al., 2007; Potter, 2018) and cannot capture upper-tropospheric conditions that impact pyroconvective outcomes (Peterson et al., 2015).

While imperfect in its application, the basic concepts of the HI are still useful. For example, Peterson et al.’s (2017a) climatology of thermodynamic profiles proximal to deep

pyroCb (i.e., plumes reaching the upper troposphere) suggests that pyroCb preferentially form in “inverted-V” profiles, similar to dry thunderstorms (<https://www.meted.ucar.edu/mesoprim/skewt/>). The inverted-V is the essence of a high HI (large dew point depression and a steep lapse rate in the lower troposphere) and implicitly implies that the air is often near saturation at the top of a deep mixed layer (due to the adiabatic cooling). This near-saturated layer aloft facilitates cloud and pyro-cloud formation, though the fate of those clouds (growing versus decaying) requires additional factors to understand, as discussed below.

A key question for plumes growing in inverted-V type environments is, “at what height will clouds form in a fire-heated column?” The answer to this question has been the topic of some debate (Potter et al., 2012), centered on the comparative roles of fire-generated heat and moisture along with the role of environmental (i.e., ambient) moisture in setting the cloud base height within the plume. Some authors have speculated that fire-generated latent heat fluxes, for example, could lower the condensation level in plumes making pyroCb initiation more likely. Luderer et al. (2009), however, show rather conclusively that moisture from combustion always plays a secondary role to the fire’s sensible heating effects and thus minimally influences condensation levels. Large-eddy simulations confirm this inference, indicating small variations in cloud base height are linked to fire latent heat fluxes (Thurston et al., 2016; Eghdami et al., 2023). Rather, the fire-plume’s condensation level is dominated by the entrained ambient moisture into the plume (e.g., the environmental mixing ratio in the lower troposphere), which helps explain why monsoonal moisture surges are often harbingers of pyroCb activity (Peterson et al., 2017b).

Observational evidence supporting the dominance of environmental moisture in setting the plume's condensation level comes from Lareau & Clements (2016), who explored the observed condensation height of smoke plumes from fires in Northern California using lidar, radar, and radiosonde data. These data show that the actual condensation level occurs near the environment's convective condensation level (CCL) and is generally much higher than the lifting condensation level (LCL). This makes sense in that the lifting mechanism in wildfires is strong heating from a fire yielding highly buoyant parcels such that the added heat makes plumes condense higher in the atmosphere than an ambient air parcel that is mechanically lifted. While a number of other recent pyroCb cases appear to confirm that the CCL remains a useful approximation (e.g., Lareau et al. 2018; Lareau et al., 2022) for pyroCb cloud bases, one of the goals of this paper is to revisit this concept in a more systematic manner across multiple pyroCb occurrences (see question 1 in the introduction).

While the CCL may be a useful estimate for pyroCb cloud base height, a more complete approach at examining pyroCb initiation and subsequent vertical development requires an assessment of how much energy must be added to an atmospheric column to initiate moist convection. Tory (2019) and Tory & Kepert (2021) developed an approach for determining the required fire power for the column to be heated enough to reach condensation and for subsequent deep moist convection to penetrate deep into the tropopause. This PyroCb Firepower Threshold (PFT) relies on an assumption that a fire's smoke plume behaves like an idealized steady-state plume in a crosswind such as described in Briggs (1975) and that the plume becomes highly diluted by entrainment of environmental air by the time it reaches condensation. Tory and Kepert's (2021) detailed

examination of the PFT, which includes an analysis of the Bald Fire pyroCb previously examined in Lareau and Clements (2016), suggests that the CCL assumption is reasonable, but that a range of condensation levels are possible depending on the entrainment rate of the plume.

Conceptually similar to the PFT, Leach & Gibson (2021) proposed a “blow up delta-T”. This approach computes how much the mixed layer must be warmed, hence the “delta-T”, to realize a sudden increase in a parcel’s equilibrium level, which is often a result of pyroCu/Cb formation causing rapid parcel ascent due to moist instability aloft (e.g., rapid plume ascent during the Carr Fire documented in Lareau et al. (2018)). Leach & Gibson (2021) showed that computing the blow up delta-T had a reasonably good correspondence to changes in fire growth during one fire (the Rice Ridge Fire), but there is a need to evaluate this approach more broadly and to find a way to merge the blow up delta-T with the potential for fire heating, such as in the PFT.

Finally, we note that while the PFT and blow up delta-T approaches may isolate periods conducive to vertical development of pyroconvective clouds, the fate of those clouds likely hinges on other processes that are not fully incorporated in the parcel-based approaches. For example, the fate of the clouds may depend on:

1. Variable entrainment rates diluting the convective core (discussed in Tory et al. (2018)).
2. Deleterious or advantageous shear profiles (e.g., tornadic pyroCbs in veering wind profiles from Lareau et al. (2022)).

3. The magnitude of the convective available potential energy (CAPE) and convective inhibition (CIN), discussed in Potter & Anaya (2015).
4. The magnitude and inertia of fire-generated updrafts in the sub-cloud layer (e.g., ~60 m/s subcloud updrafts documented by Rodriguez et al. (2020)).

These co-variations in pyrocloud fate and environmental conditions suggest that it is necessary to consider both the meteorological context and the fire heating processes at the surface to arrive at a useful prediction of when and where pyroCb will form. In the following case study of the Bootleg Fire, we rely on remote sensing datasets and other easily accessible data, such as radar and numerical weather models, to characterize wildfire plume dynamics and examine potential frameworks for pyroconvective forecasting and now-casting. We apply the methodologies detailed in Lareau & Clements (2016), Tory & Kepert (2021), and Briggs (1975) to the Bootleg Fire to evaluate this variability in pyroconvective behavior.

3. Data and Methods

3.1 The Bootleg Fire

The lightning-ignited Bootleg Fire was discovered on 6 July 2021 and went on to burn over 413,000 acres of south-central Oregon's Fremont-Winema National Forest (Fig. 2). A combination of exceptional drought conditions spanning the previous two years with record high temperatures in 2021 preceded the aggressive fire (Alaska Incident Management Team, 2021).

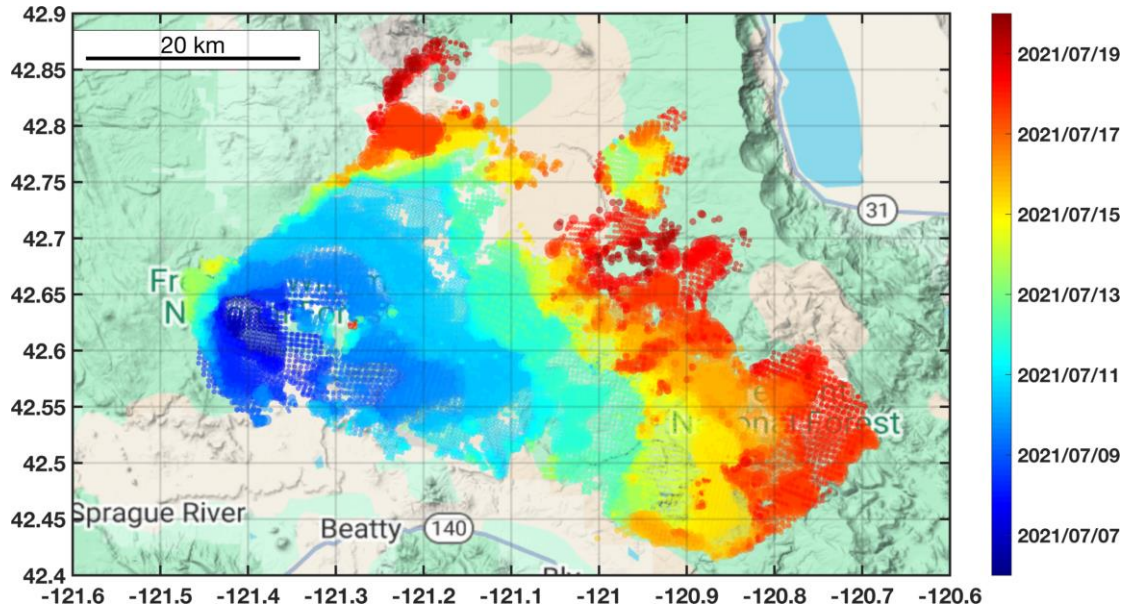


Figure 2 Summary of the Bootleg Fire's spread based on VIIRS hot-spot detections. The color of the markers indicates the date of the detection and the size of the marker the relative fire intensity (measured in terms of the Fire-Radiative Power (FRP)).

From 6-18 July, the Bootleg Fire presented day-to-day variability in pyroconvective behavior, ranging from dry convective plumes to days culminating in moist convective clouds spanning the spectrum of shallow pyroCu, deep pyroCu, and pyroCb. Amongst the pyroCb-producing days a range of pyroCb characteristics occurred, including brief pyroCb “puffs”, sustained pyroCb, and detraining cirrus anvils, rain and lightning-producing pyroCbs, and one case of a tornadic vortex linked to a pyroCb. This wide range of convective outcomes from a single fire provides a unique opportunity to probe the factors controlling the variations in plume and cloud development.

3.2 Analysis Approach

To assess the fidelity of pyroCb predictive tools during the Bootleg Fire we require three primary pieces of information:

1. The ambient thermodynamic environment.
2. The fire's size and intensity, and thus the total heating.
3. Time-resolved documentation of the pyroconvective outcomes, ranging from non-pyroCu/Cb plumes to deep pyroCb producing precipitation and lightning.

Below we detail how we arrive at these pieces of data.

3.2.1 Model Data

The High-Resolution Rapid Refresh model (HRRR; Dowell et al., 2022) is used to determine the thermodynamic and wind structure of the atmosphere around the Bootleg Fire. Initialized hourly and spatially resolved at 3km, the HRRR enables an analysis of the Bootleg Fire at high spatial and temporal scales. Variables gathered from this data include:

1. Mixed layer wind speed (U_{ML}), calculated as the average wind from the ground to the CCL, reflecting the dry portion of the plume. U_{ML} provides information about winds impacting the plume rise such as Tory & Kepert (2021) use for computing the PFT.
2. CCL height, a useful indicator for the height at which a plume will condense (Lareau & Clements, 2016).
3. Convective temperature and convective parcel path, which are used to compute the “fire” convective inhibition (Fire CIN) and convective available potential energy (Fire CAPE), described later in this paper.
4. Height of critical temperature levels, such as the homogeneous freezing level (-38°C), the -20°C height, and the cold-point tropopause height.

3.2.2 Satellite Data

PyroCu/Cb detection: The Advanced Baseline Imager (ABI) aboard the GOES-17 satellite is used to detect pyroCu and pyroCb using the 0.64 μm “red” albedo and cloud-top temperatures (via the 10.3 μm “clean” infrared (IR) band), respectively. PyroCu are identified using an adaptive albedo threshold (α_{min}) to identify bright white cloud elements over the fire. Pixels meeting or exceeding the threshold are flagged as pyroCu. The adaptive threshold, defined by,

$$\alpha_{min} = (0.0672 * \ln(\Delta t + 3)) + 0.0296$$

is a function of the minutes (Δt) until sunset (~03:45 UTC), to account for decreasing solar incidence angle and thus less bright cloud features later in the day. This approach is tuned for the time of year and latitude of the Bootleg Fire and is not intended to be universally applicable at all latitudes and times of year.

Fig. 3a,c provide an example of our pyroCu detection from the 0.64 μm ABI band on 10 July during a developing pyroCu/Cb pulse. Note the magenta dots in Fig. 3c correspond to the bright white cloud features in Fig. 3a. To ensure we do not include “ordinary” cumuli not influenced by the fire, we restrict pyroCu detections to occur within the radar-defined plume boundaries (further described below), which are displayed as black contours (Fig. 3c). For each timestep, we then count the number of pyroCu pixels.

PyroCb detection is based on the presence of cold, glaciated cloud tops. Specifically, IR pixels below -20°C (253 K) are flagged as pyroCb. While the exact behavior of ice nucleation in condensing wildfire plumes remains unclear (McCluskey et

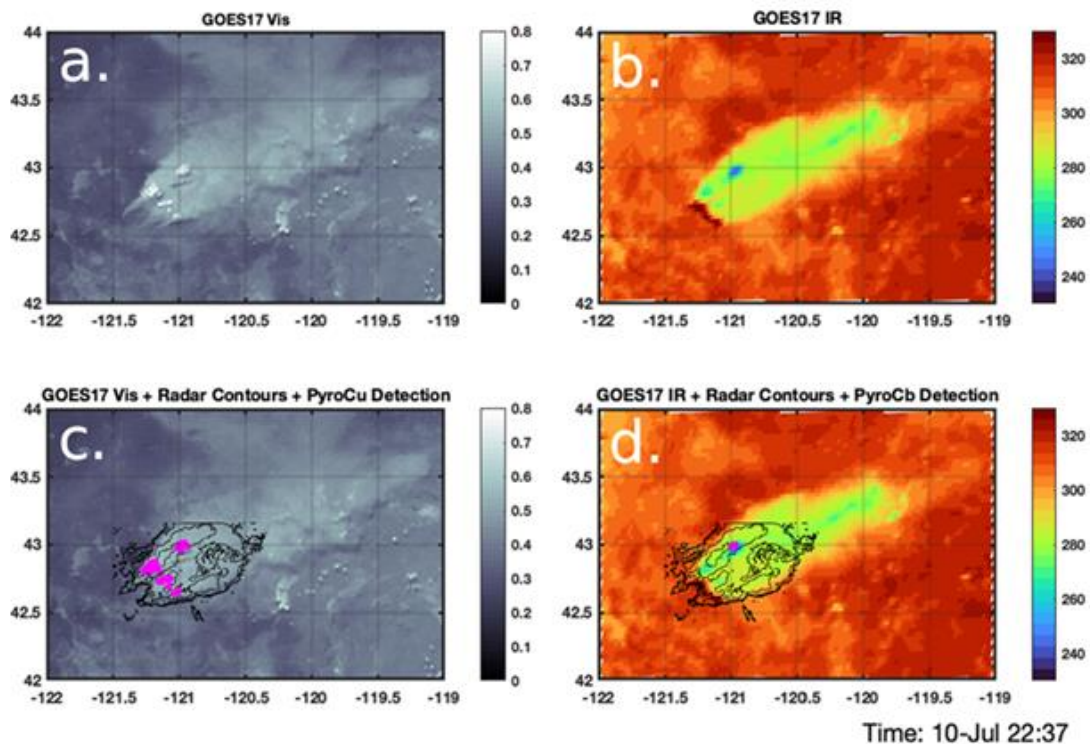


Figure 3 (a) GOES “Red” visible imagery with a pyroCb “puff” detached from the updraft at 22:37 UTC on 10 July, (b) GOES longwave IR, (c) radar contours and pixels flagged as pyroCu (magenta) based on the adaptive albedo threshold, and (d) radar contours and pixels flagged as pyroCb (magenta).

al., 2014; Barry et al., 2021), this temperature threshold is aligned with the Tory’s (2019) PFT and is generally inclusive of deep or towering pyroCu en route to becoming pyroCb reaching the upper troposphere. We also count pixels less than -38°C (235 K), corresponding to the homogenous nucleation temperature, which is a widely used threshold in satellite classification of pyroCb (Peterson et al., 2017a). An example of our temperature thresholding and detection is provided in Fig. 3b,d, where the magenta pixels in Fig. 3d correspond to sufficiently cold ($<-20^{\circ}\text{C}$) pixels in Fig. 3b. Once again, we restrict the pyroCb features to occur within the radar derived plume boundaries.

We note that the pyroCu pixels determined from the visible channel have a finer resolution (0.5km) than IR-based pyroCb pixels (2km). This difference means that we'd expect pyroCu pixel counts and pyroCb pixel counts to differ by a factor of 16 for a given pyroCb occurrence.

Fire characterization: GOES-17's ABI data are also used to characterize the location and intensity of the Bootleg Fire using the Fire Detection and Characterization Algorithm (FDC) (Schmidt et al., 2020). The FDC product is primarily driven by the 3.9 μm shortwave IR brightness temperature (BT), which is near the peak of thermal emissions from fires and employs a number of other algorithmic checks based on visible and IR bands.

Outputs of the FDC algorithm include detected fire pixels and Fire Radiative Power (FRP), which is the estimated total radiant energy emitted from the pixel (in units of Watts), and thus a measure of the instantaneous intensity of a wildfire. There are two primary limitations to the GOES FRP product that must be overcome. First, the 3.9 μm channel saturates for intense fires, and FRP values are not reported for these saturated pixels. This is problematic in that the FRP product is thus missing the most intense part of the fire, which is often the driver for pyroCb development. Second, once pyroCu/Cb form, the algorithm sometimes reports "cloud-contaminated" pixels due to the cold cloud tops affecting the background values of adjacent IR brightness temperatures.

We bypass these issues in two ways. First, we fill saturated pixels with an assumed large FRP value (3,000 MW) which is slightly above the typical values just prior to saturation (e.g., ~2,600 MW). This results in a conservative estimate of the actual total FRP

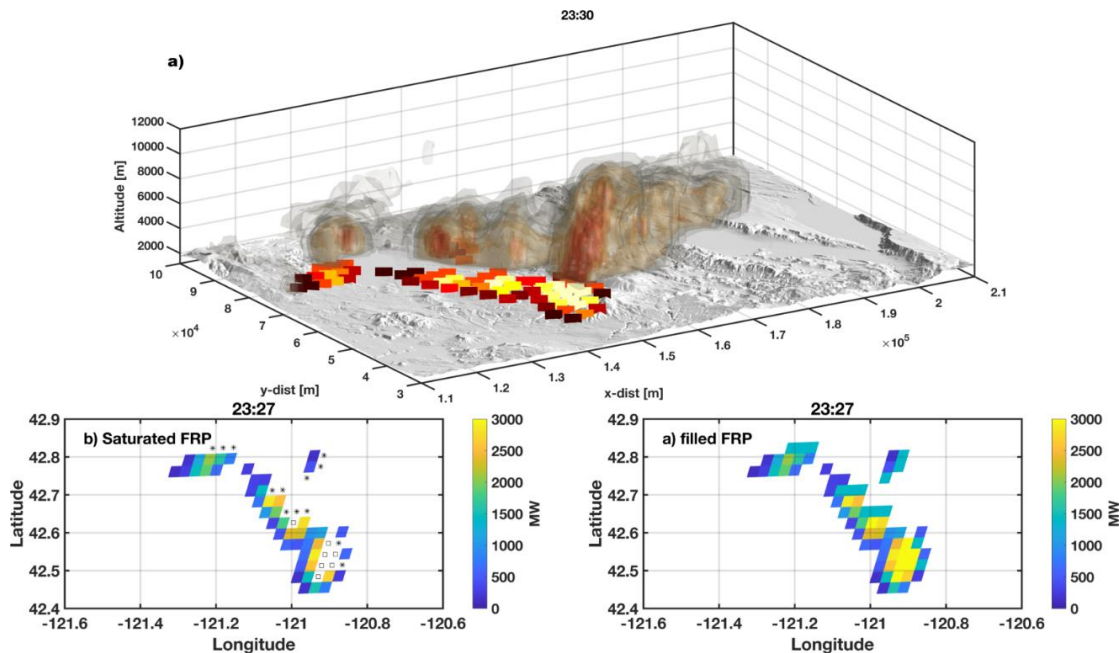


Figure 4 (a) 3-D reconstruction of the Bootleg Fire’s smoke plume on 14 July 2021 at 23:30 UTC using data from the KMAX NEXRAD radar. GOES FRP pixels from the FDC on 14 July 2021 22:37 UTC.

Displayed pixels are (b) raw data from GOES-17, and (c) corrected for saturation and cloud-contamination. Saturated pixels are filled with 3,000 MW and cloud-contaminated pixels are filled using a regression analysis between $3.9 \mu\text{m}$ BT’s and FRP values for non-cloud-contaminated, non-saturated pixels.

during high-intensity fire periods but avoids extrapolation. Second, we estimate cloud-contaminated pixel FRP using a regression analysis between the raw $3.9 \mu\text{m}$ brightness temperature and FRP values for non-cloud-contaminated, non-saturated pixels. An example of these filling procedures for a period with both saturated and cloud-contaminated pixels is shown in Fig. 4c. Note that the southeastern portion of the fire is producing the deepest plume but in the unfilled data has only a few FRP points. The filled data in contrast show local maxima in FRP linked to deep plumes evident in the radar data.

3.2.3 Radar Data

Observations of plume height, structure, and equivalent reflectivity were obtained from the Medford, Oregon (KMAX) National Weather Service's (NWS) Next Generation Weather Radar (NEXRAD), located roughly 120km southwest of the Bootleg Fire. The 10-cm wavelength of these radars detects large hydro- and pyro-meteors within wildfire smoke plumes (McCarthy et al., 2019). Similar to other recent analyses (Lareau et al., 2022), we re-grid the radar data from its native polar coordinate to a cartesian grid with a grid spacing of $dx=dy=dz=500\text{m}$. The gridded data facilitate averaging and comparisons despite occasional changes in the radar's scan parameters (i.e., different volume coverage patterns, VCP's). NEXRAD data is beneficial in this study for our ability to visualize smoke plume cross-sections and 3-D reconstructions, allowing for a volumetric analysis of the plume. One such example of a 3-D reconstruction is presented in Fig. 4a, which is close to the time of the FRP data shown above. Note the plume elements rising from the long, active flank of the fire and the deeper plume with larger reflectivities rising from the most active southeastern part of the fire front.

4. Results

4.1 Overview of the Bootleg Fire's Plume

We begin our analysis by summarizing the inter- and intra-day plume development and pyroconvective outcomes spanning the Bootleg Fire's most active period of 6-19 July 2021 (Fig. 5). This period captures regular diurnal variations in fire activity and plume development as well as a spectrum of convective outcomes spanning dry convective plumes, shallow pyroCu, and deep pyroCb. This variability is apparent in Fig. 5a which

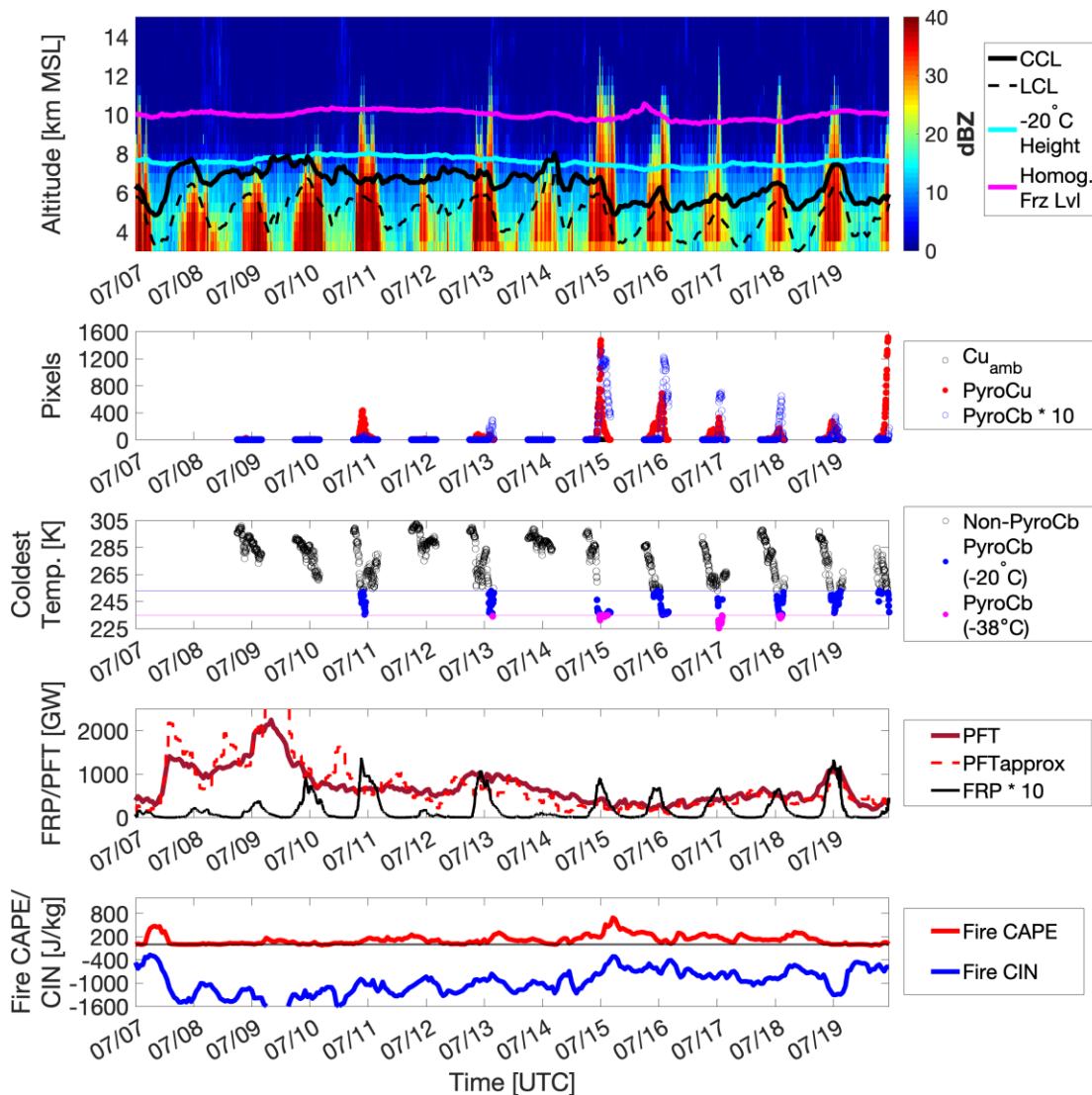


Figure 5 (a) Maximum reflectivity (shaded), CCL height (black line), LCL height (dashed black line), -20°C temperature height (cyan line) which is the cloud top temperature where we quantify pyroCb, and the homogeneous freezing level (magenta line). (b) Number of pixels detected from GOES-17 for Cuamb (black), pyroCu (blue), and pyroCb (red, multiplied by 10). (c) Lowest cloud-top temperature, divided into non-pyroCb temperatures (black), pyroCb temperatures based on the -20°C threshold (blue), and temperatures at or below the homogenous freezing level (magenta). (d) PFT (dark red) and PFT_{approx} (dashed red) overlaid on top of the FRP_{x10} (black). (e) Fire CAPE (red) and Fire CIN (blue).

presents a time-height diagram of the maximum in radar reflectivity (dBZ) in the Bootleg Fire plume. Present in these data are variability in the magnitude of dBZ (e.g. contrast 15 July against 16 July), plume depth (e.g. contrast 13 July against 14 July), and the plume's diurnal cycle. This diurnal variability manifests as high dBZ and deep plume top heights

during afternoons contrasting with low dBZ and plume top heights during nights and mornings. Despite this consistent diurnal pulsing of the fire and plume, the extent of the plume's day-to-day activity varies, with some days experiencing comparatively low reflectivity and plume depth and others experiencing high reflectivity or deep plumes linked to pyroCb.

To determine when the plume is producing pyroCu/Cb, we overlay the radar time-height data with the CCL height (thick black line), the LCL height (thin black line), the -20°C height (cyan line), and the homogenous freezing level (-38°C , magenta line). These levels are chosen to represent the approximate height of the cloud base (i.e., the CCL as suggested from Lareau & Clements (2016)) along with transitions to mixed phase and glaciated clouds, and thus help distinguish between periods with dry plumes and those with pyroCu/Cb. Notably, the Bootleg Fire exhibited days in which the radar-observed plume top exceeded one (e.g. 9 July) or both temperature levels (e.g. 10 July), only the CCL height (e.g. 11 July), or none of these critical heights (e.g. 13 July), providing an opportunity to assess the factors controlling pyroCu/Cb development.

We also examine satellite-derived pyroCu/Cb pixel detections (Fig. 5b). Note, the pyroCb pixel counts are scaled by ten for improved visibility in the plot. Complimenting the pixel counts, we also examine the minimum IR cloud-top temperature in the Bootleg Fire's plume (Fig. 5c). Recall, pyroCb pixels (i.e., red markers in Fig. 5b) are those whose temperature drops below -20°C , which are likely to contain mixed-phase or glaciated clouds. We also record when the plume-top temperature reaches the homogenous freezing

level (shown in magenta points in Fig. 5b), the point at which the plume must be glaciated, and thus a de facto pyroCb.

In inspecting Fig. 5a-c we find a strong relationship between the extension of the radar-observed plume above the CCL and the presence of pyroCu/Cb pixels. For example, on 14 July (local time) the radar-derived plume top surpassed and sustained extensive depth above the CCL through the afternoon. On this day, the fire produced the maximum number of pyroCu/Cb pixels in our study period with sustained cloud-top temperatures below the homogeneous freezing level. This contrasts with the plume and cloud development on 9 July, wherein the plume minimally exceeds the CCL. Correspondingly, the plume produces pyroCu, but no pyroCb was detected. More broadly, most days either have a plume which does not reach the CCL, corresponding to no moist convective clouds (e.g., 7, 8, 9, 11, and 13 July), or a plume that substantially exceeds the CCL and generates deep convection (all other days). This behavior hints at the non-linearity in plume growth due to moist convective initiation.

Importantly, these analyses also indicate that the plume's exceedance of the CCL is a much better discriminator of pyroCu/Cb development than the exceedance of the LCL. Note that the plume tops exceed the LCL every day, yet clearly not every day produces pyroconvection. While this is not surprising, these simple results should provide clear justification for excluding LCL-based approaches in pyroconvective forecasting, excepting the case where the LCL and CCL are nearly the same (i.e., days that support widespread convection). We further support and detail these observations in the following section.

3.2 Using the CCL to identify pyroCu development

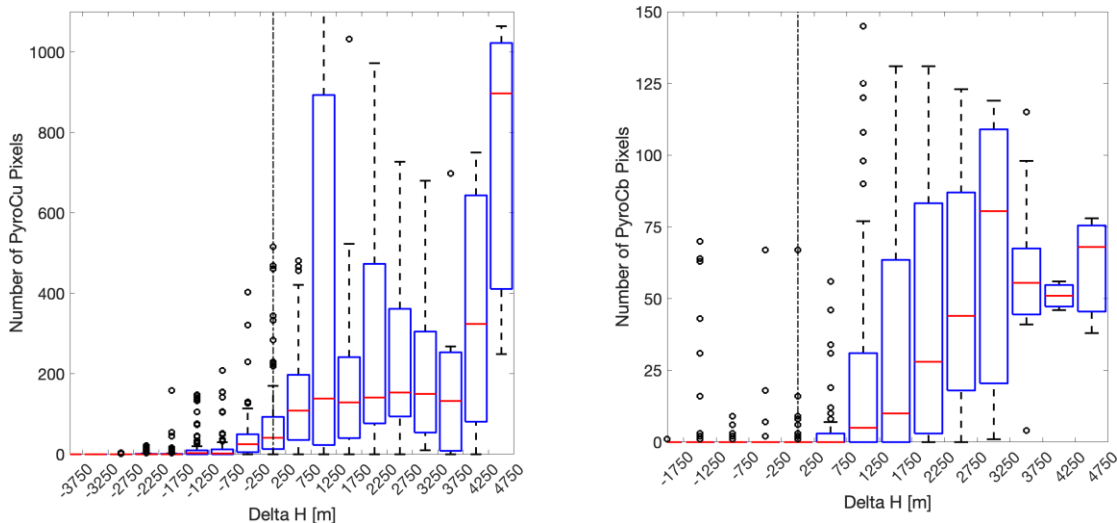


Figure 6 Distributions of plume top height minus the CCL (ΔH) for (a) pyroCu and (b) pyroCb.

To quantify the relationship between pyroCu/Cb initiation and smoke plume exceedances of the CCL apparent in Fig. 5a-c, we examine the difference in height (ΔH) between the radar-derived plume top (using a 20 dBZ threshold) and the CCL (Fig. 6). These data show that as ΔH exceeds zero (i.e., the plume top surpasses the CCL) the number of pyroCu pixels increase, becoming progressively larger with increasing ΔH values (Fig. 6a). This finding is consistent with the results from Lareau & Clements (2016), and more broadly establish the usefulness of the CCL in pyroconvective forecasting. Also of note, Fig. 6b shows that ΔH of $\sim 1,000$ m tends to correspond to pyroCb initiation. This level may correspond to a freezing level at which condensed plumes begin to glaciate and release additional latent heat (i.e., the heat of fusion). While large ΔH values are likely required for deep pyroCb to form, we expect that other aspects of the environment impact the extent of cloud growth.

4.2 Fire CAPE and Fire CIN

We also examine variations in CAPE and CIN as it relates to the observed pyroconvective outcomes by adapting Doswell & Rasmussen's (1994) CAPE formulation and implementing a similar modification as Potter & Anaya (2015) where they begin calculating CAPE at the level of free convection (LFC) as opposed to the surface. In this calculation, henceforth referred to as Fire CAPE, the level of free convection is equivalent to the CCL and integration below this height is considered convective inhibition, henceforth referred to as Fire CIN. Therefore, Fire CIN quantifies the energy needed to be added to the environment below the CCL for a fire-heated air parcel to rise to the CCL. The resulting formulas are,

$$Fire\ CIN = g \int_{Z_{SFC}}^{Z_{CCL}} \frac{(T_{v,par} - T_{v,env})}{T_{v,env}} dz$$

$$Fire\ CAPE = g \int_{Z_{CCL}}^{Z_{EL}} \frac{(T_{v,par} - T_{v,env})}{T_{v,env}} dz$$

where g is gravity (9.81 m/s), and Z_{SFC} , Z_{CCL} , and Z_{EL} are the surface elevation and the heights of the CCL and EL, respectively. $T_{v,par}$ and $T_{v,env}$ represent the virtual temperatures of the convective parcel and the environment, respectively, at all pressure levels within the HRRR model.

The hourly variations in Fire CAPE/CIN are shown in Fig. 5e and Fig. 7. Broadly speaking, there are two phases of the Bootleg Fire with differing Fire CAPE/CIN distributions that are loosely linked to the variations in pyroCb frequency. First, from 7 July to 14 July, high Fire CIN (>1,000 J/kg during active fire periods) and low Fire CAPE

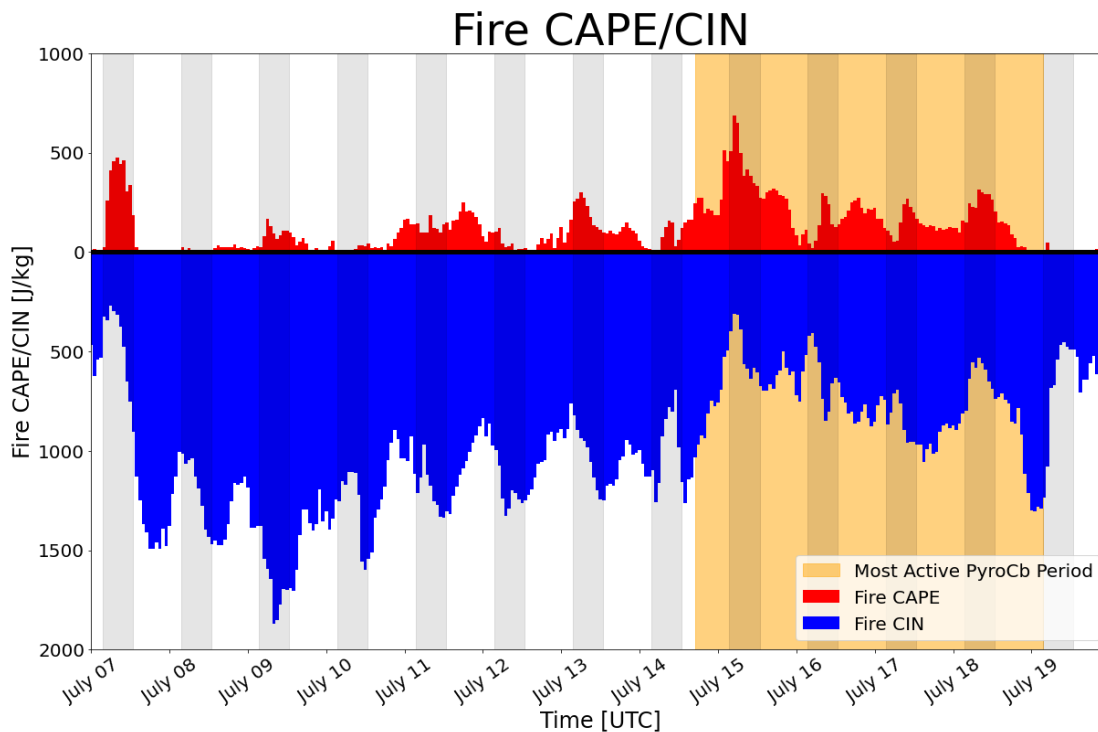


Figure 7 Fire CAPE (red) and Fire CIN (blue) values overlaid on top of the most active pyroCb period (shaded yellow).

(<310 J/kg during active fire periods) are observed. This period has comparatively few pyroCb detections. Second, from 14 to 18 July, Fire CIN drops below 1,000 J/kg and Fire CAPE is more consistently positive, including a peak of over 500 J/kg after sunset on 14 July. This period has numerous pyroCbs. Referring again to Fig. 5a, it is clear that the primary driver in these two thermodynamic regimes is the abundance or scarcity of lower tropospheric humidity, which is apparent in terms of the CCL: the higher CIN, lower CAPE periods have appreciably higher CCLs due to lower water vapor mixing ratios (all else being equal).

It is tempting to conclude from this analysis that Fire CAPE, Fire CIN, and pyroCbs are cleanly linked together, but closer inspection of the data suggests that there is a more

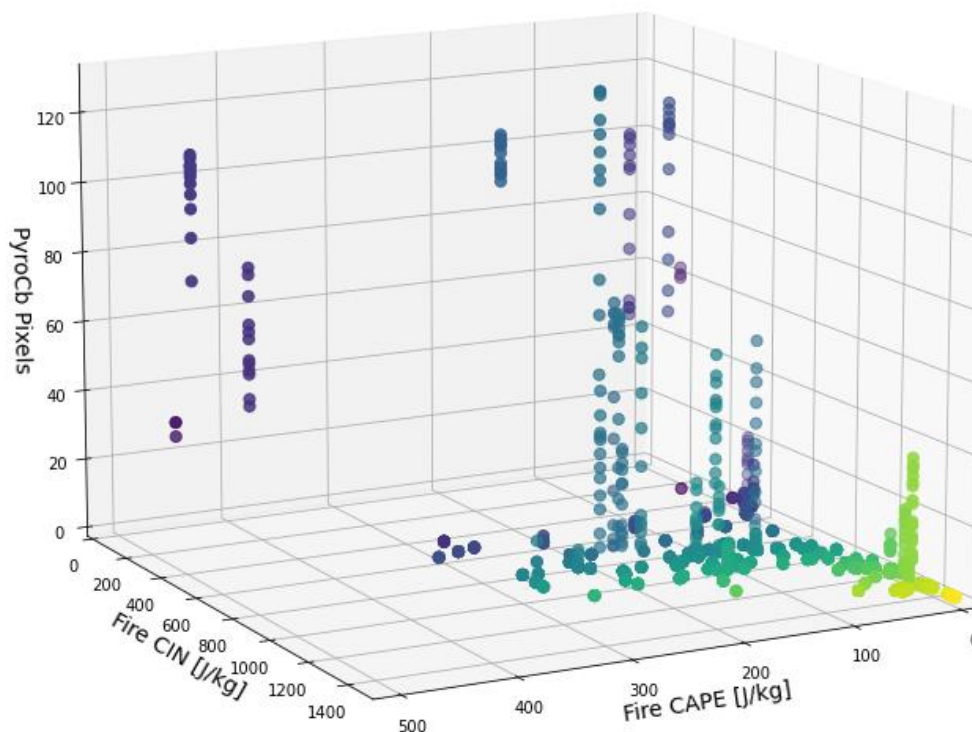


Figure 8 Number of pyroCb pixels detected given values for Fire CAPE and Fire CIN (shaded).

complex and nuanced relationship. This is particularly apparent on the late afternoon of 18 July, when Fire CAPE dropped to about zero while Fire CIN rose to over 1,200 J/kg. Counter to expectations, this period was characterized by notable pyroCb activity, including a pyrogenic tornado.

To probe the nature of this relationship, we plot Fire CAPE and Fire CIN against pyroCb pixel counts at corresponding times in Fig. 8. These data indicate that pyroCb can, and do, form in a range of stability regimes. At one end of this parameter space, the 18 July case produces 40 pyroCb pixels with Fire CIN exceeding 1,300 J/kg and Fire CAPE of ~ 0 J/kg. At the other end of the parameter space, on 15 July ~ 100 pyroCb pixels occur during

a period with low Fire CIN (<200 J/kg) and high Fire CAPE (>400 J/kg). In between these extremes, pyroCb occur within a range of Fire CAPE/CIN values. These data suggest that there are multiple pathways to pyroCb, rather than a single conducive thermodynamic environment.

We reinforce this point by comparing and contrasting the thermodynamic profiles (i.e., skew-T diagrams) for the end-member pyroCb cases (Fig. 9). On 18 July while there is ~ 0 CAPE above the CCL, the convective parcel is approximately neutrally buoyant through a deep layer (up to ~ 300 hPa, Fig. 9b). Thus, while the pyroCb that formed in this environment lacks a strong contribution from latent heating in accelerating the updrafts aloft, there was little resistance to the fire-heated parcels rising through a deep condensed layer. Fig. 4d shows that this pyroCb occurred during a period of very high FRP (the second highest in the fire's evolution), suggesting the fire-heating was sufficient to overcome the large fire-CIN, and generate very strong sub-cloud updrafts (e.g., the extreme sub-cloud updrafts reaching ~ 60 m/s observed by Rodriguez et al. (2018)) that rise through the deep layer via inertia. This scenario could be thought of a "forced pyroCb".

In contrast, on the afternoon/evening of 14 July, the thermodynamic profile indicates comparatively large fire CAPE with parcel temperatures becoming significantly warmer than the environment as a consequence of latent heating aloft (Fig. 9a). This parcel is thus likely to experience reinvigorated updrafts aloft due to the additional buoyancy, whereas the previous example on 18 July would not. Note this environment also has less fire CIN, and likely has smaller fire-generated updrafts. This scenario could be thought of as an "active pyroCb".

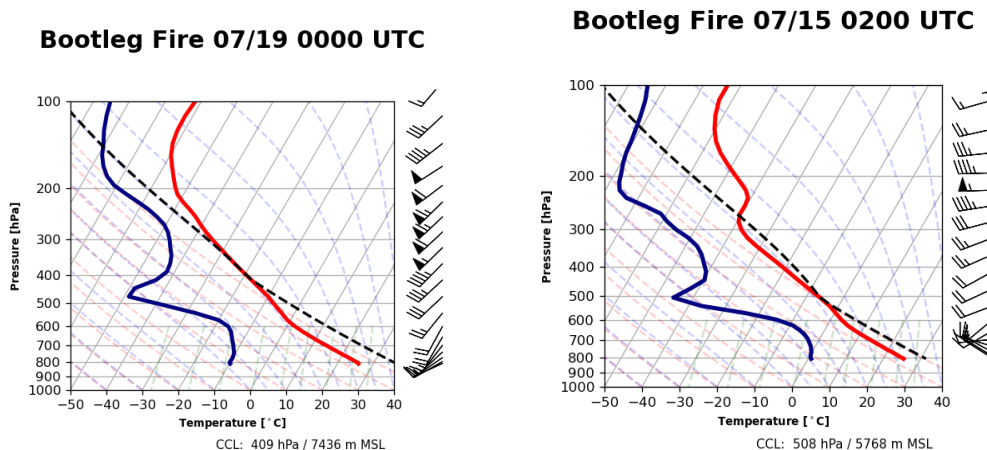


Figure 9 Skew-T diagrams from (a) 02:00 UTC on 15 July, and (b) 00:00 UTC on 19 July. The solid red and blue lines represent temperature and dewpoint, respectively, while the dashed black line represents a convectively lifted parcel temperature.

Based on these analyses, we propose that it is useful to conceive of two pathways to pyroCb formation. The first pathway has low Fire CAPE and high Fire CIN (Low-High). Here, high energy fires (i.e., large FRP) force plumes to heights capable of glaciation, such as in Fig. 9b. These might be thought of as “bottom” heavy plumes in that the fire heating is the dominant driver. The second pathway is a high Fire CAPE, low Fire CIN (High-Low) environment. Here, a more modest amount of fire heating initiates a cloud, which becomes actively convective aloft. These could be thought of as “top heavy” plumes, with larger contributions from latent heating aloft. Indeed, previous investigations suggest similar concepts, such as Leach & Gibson (2021) who examine the ratio of fire-generated and moist buoyancy. An additional takeaway from this analysis is that Fire CAPE and Fire CIN are likely most useful when paired with FRP as evidence suggests no specific combination of values for these indices are optimal for pyroCb formation. Rather, fire-heating is a critical consideration, which is the focus of the next section.

4.3 Fire Power Threshold

The PFT approach explicitly examines how much fire heating is required to initiate deep moist convection, and thus combines the concepts discussed above (i.e., condensation levels, CIN, and CAPE). The PFT is defined as

$$PFT = \left[\pi C_{pd} \left(\frac{\beta'}{1 + \alpha' \beta'} \right)^2 \right] * \rho_0 * Z_{fc}^2 * U_{ML} * \Delta\theta_{fc}$$

The leading term of constants, $\left[\pi C_{pd} \left(\frac{\beta'}{1 + \alpha' \beta'} \right)^2 \right]$, contains the specific heat of dry air (C_{pd}), the internal plume entrainment parameter (β'), the fraction of the plume's radius below the level of free convection (α'), and the plume and environmental constant density (ρ_0). Tory and Kepert (2021) indicate that in most instances this group of constants can be approximated as $397.3 \text{ J kg}^{-1} \text{ K}^{-1}$. Additional details of these coefficients are provided in Tory and Kepert (2021). The remaining portion of the PFT contains environmental variables Z_{fc} , U_{ML} , and $\Delta\theta_{fc}$. Z_{fc} is the height of the level of free convection in meters, U_{ML} is the mean mixed layer wind speed in meters per second, and $\Delta\theta_{fc}$ “defines how much warmer than θ_{ML} the plume needs to be for free convection to develop” (Tory & Kepert, 2021), where θ_{ML} is the mixed layer potential temperature. In our application, all inputs to compute these environmental variables are determined using HRRR data.

Fig. 5d presents the PFT and the scaled FRP (i.e., FRP_{x10}). FRP_{x10} approximates the fire's sensible heating as a constant multiple of the radiant energy (Val Martin et al., 2012) such that when FRP_{x10} exceeds the PFT pyroCb are expected to form. Indeed, inspection of the panels in Fig. 5 suggests that as the fire heating exceeds the PFT

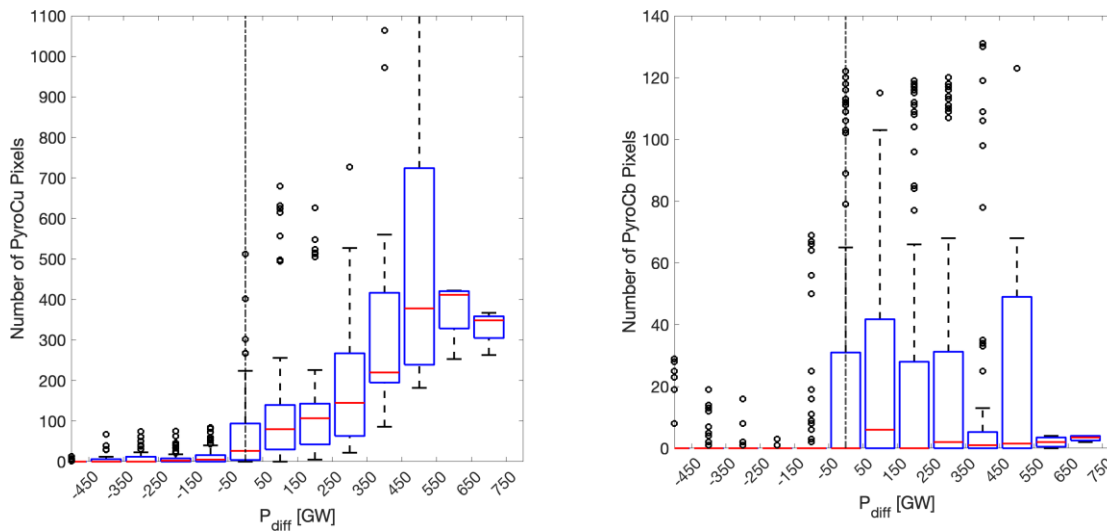


Figure 10 The difference between FRP_{x10} and PFT for (a) pyroCu and (b) pyroCb.

convection commences, measured in terms of plume depth/temperature and pyroCu/Cb pixel counts. Note for example on 10 July the first time the FRP_{x10} passes the PFT, rapid plume deepening and pyroCb initiation occur.

To quantify this relationship, Fig. 10 presents the number of pyroCu (Fig. 10a) and pyroCb (Fig. 10b) pixels at incremental differences (P_{diff}) between the FRP_{x10} and the PFT. The results are clear: as P_{diff} becomes positive pyroCu and pyroCb occurrences are “switched on”. For pyroCu (Fig. 10a), the number of pixels increases with increasing P_{diff} , with maximum pyroCu counts for ~400 GW of P_{diff} . PyroCb pixel counts (Fig. 10b), in contrast, do not monotonically increase with increasing P_{diff} and median pyroCb counts hover around zero, indicating that even when the PFT is exceeded only about 50% of the time are pyroCb observed during the Bootleg Fire. Thus, like many convective parameters, PFT exceedance is likely a necessary but insufficient condition for pyroCb formation, with other limiting factors influencing the fate of developing clouds.

We also test this relationship for a simplified PFT (hereafter $PFT_{approx.}$) given by,

$$PFT_{approx} = [397.3 \text{ J K}^{-1} \text{ kg}^{-1}] * \rho_0 * Z_{CCL}^2 * U_{CCL} * \Delta\theta_{CCL}$$

where we use Z_{CCL} (the height of the CCL) in place of Z_{fc} , U_{CCL} (the wind speed averaged from ground level to the CCL) in place of U_{ML} , and $\Delta\theta_{CCL}$ (the increment to reach the mixed-layer convective temperature) in place of $\Delta\theta_{fc}$. These approximations are used because:

1. We've established that the CCL is a useful and simple approximation for the plume condensation level (Fig. 5).
2. These variables are readily available to forecasters without explicit computation of the PFT.

As summarized in Fig. 11, the PFT_{approx} results mimic the PFT, with pyroCu (Fig. 11a) and pyroCb (Fig. 11b) detections mostly occurring when the FRP_{x10} exceeds the PFT_{approx} . PFT_{approx} is also shown in Fig. 5d, where it is clear that its day-to-day variations agree well with the PFT, though there are larger fluctuations on diurnal timescales. From

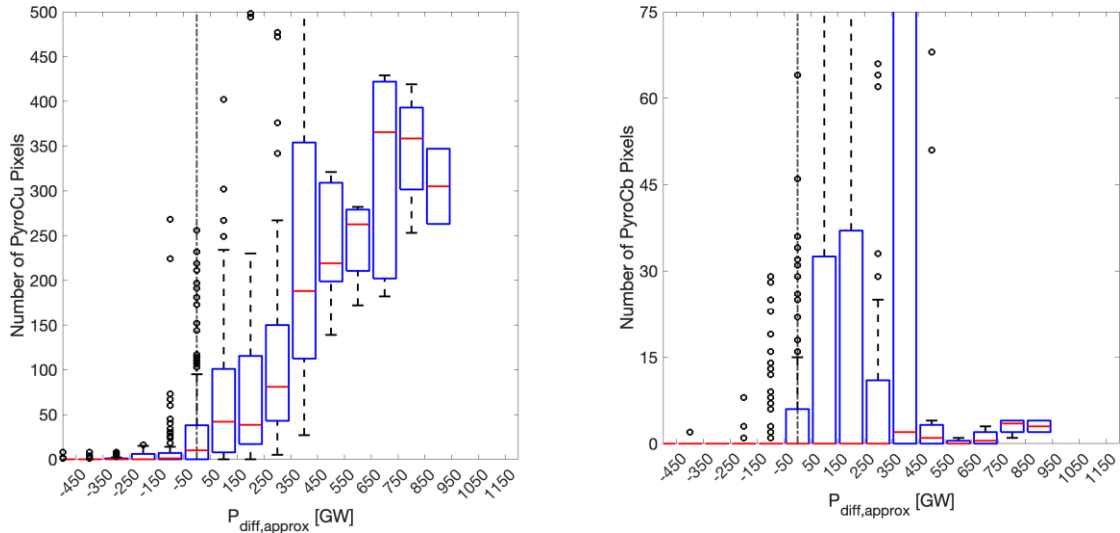


Figure 11 The difference between FRP_{x10} and PFT_{approx} for (a) pyroCu and (b) pyroCb.

these results we conclude PFT_{approx} could provide a valuable and easy to apply tool for forecasting of pyroCb, especially in combination with observations of FRP.

It is useful to return to the contrasting Fire CAPE and CIN pyroCb cases in Fig. 9, but to now include FRP_{x10} and PFT values, which are summarized in Table 1. We note that the High-Low scenario corresponds to a case with lower CCL heights and less required fire heating for cloud development (i.e., small $\Delta\theta$) due to somewhat moister ambient conditions. Noting that the PFT is directly proportion to these variables, this case thus has a relatively low PFT of (326 GW). In contrast, the 18 July Low-High scenario has a high CCL and requires more fire heating (i.e., large $\Delta\theta$), thus the PFT is much higher (1070 GW). Thus, the low PFT case might be considered an “easy to initiate pyroCb” period, whereas the high PFT case would require much larger fire heating. Indeed, the easy to initiate case had about half as much observed FRP (791 GW) as compared to the intense fire heating (1,279 GW) during the hard to initiate case, yet both days clearly produced pyroCb. Herein lies the value of the PFT: we can directly relate the required fire heating (FRP) to the observed fire heating (FRP_{x10}) and assess the pyroCb likelihood. In this framework, a forecaster

might monitor the diurnal increase in FRP to assess when the fire is reaching a critical convective threshold. We also note both scenarios presented in Fig. 9 exhibit weakened inverted-V thermodynamic profiles with a shallower well-mixed layer which results in a larger dew point depression in the mid-troposphere (roughly the 600-700 hPa layer in Fig. 9) than seen in typical inverted-V profiles. These types of soundings are climatologically expected in high-altitude pyroCb cases (Peterson et al., 2015; Peterson et al., 2017a). Low-level atmospheric characteristics in inverted-V soundings are hot and dry, as expected in high-intensity wildfires. However, these conditions will also always increase the PFT through heightened Z_{fc} and $\Delta\theta_{fc}$, as previously noted. Thus, atmospheric conditions which exacerbate wildfire intensity inherently also inhibit pyroCb production, and vice versa.

Table 1 Fire CAPE, Fire CIN, PFT, and FRP_{x10} on 15 July at 02:00 UTC (corresponding with the skew-T diagram displayed in Fig. 9a) and on 19 July at 00:00 UTC (corresponding with the skew-T diagram displayed in Fig. 9b).

Day	Fire CAPE [J kg⁻¹]	Fire CIN [J kg⁻¹]	PFT [GW]	FRP_{x10} [GW]
02:00 UTC 15 July	682.4	529.5	326	791.2
00:00 UTC 19 July	13.8	1,301.8	1,070	1,279.0

4.4 Plume Geometry

While we showed that PFT exceedance is required for pyroCb formation (e.g., Figs. 10b, 11b), we also found that it was not a sufficient condition for pyroCb growth on its own, with only about 50% of exceedance cases yielding persistent cold cloud tops. This suggests other processes impact pyroCb development, vigor, and longevity. Moreover, larger positive values of P_{diff} do not imply more widespread pyroCb (i.e., pixel counts don't strictly increase with increase P_{diff} as observed in Fig. 10b). One

hypothesized mechanism impacting pyroCb behavior is the geometry of the plume as it approaches and surpasses the CCL (e.g., Tory and Kepert, 2021), with more upright plumes more conducive to cloud development. To test this hypothesis, we examine the updraft geometry of the Bootleg Fire’s plume on selected pyroCb-producing days. We assess the geometry using the Briggs’ plume rise equation, which is one of the core assumptions of the PFT,

$$Z = C * \left(\frac{F^{\frac{1}{3}}}{U_{ML}} \right) * x^{\frac{2}{3}}$$

Where C is a constant of the form $\frac{3}{2\beta^2}$, wherein β is an empirical entrainment parameter. The recommended value for C is 0.6. The height of the plume core (Z) at distance downstream of the fire (x) in meters is thus dependent on the ratio of $\frac{F^{\frac{1}{3}}}{U_{ML}}$, where F is the buoyancy flux into the base of the plume, which is driven by the heat flux and the radius of the fire heat source along with environmental constants. In essence, the $\frac{F^{\frac{1}{3}}}{U_{ML}}$ ratio (hereafter shortened to F/U) quantifies the concept of the “power of the fire versus power of the wind,” which appears in Byram’s Convective Number, also known as Byram’s Energy Criterion (Byram, 1959), and the Convective Froude Number (Clark et al., 1996a; Clark et al., 1996b). Traditionally, this ratio was used to differentiate “plume-driven” versus “wind-driven” fires. Authors have suggested that when the ratio exceeds 1, the power of the fire overwhelms the power of the wind resulting in upright convective columns and erratic fire behavior, hence heightened safety concerns (Morvan & Frangieh, 2018). While conceptually useful, the operational usefulness and ability to quantify these

terms is not well-established (Sullivan, 2007). Regardless, the “power of the fire versus power of the wind” idea remains a common concept in wildfire plume dynamics.

In the case of the Briggs’ plume rise Equation, the F/U ratio modulates the uprightness of the plume. The stronger the fire or the weaker the wind in the mixed layer, the quicker the plume rises, or the more upright the plume is (i.e., Z increases quicker in Eq. 6 for increasing values of x), and vice versa. This allows us to evaluate the power of the fire versus the power of the wind as a continuum, ranging from bent over to upright plumes based on the F/U ratio as opposed to a breaking point used to distinguish plume-versus wind-driven wildfires.

Using this concept, the following three analyses of pyroCb-producing days provide insight into how the plume geometry may dictate pyroCb behavior. For each day’s analysis, a table presenting maximum FRP_{x10} within the 60 minutes preceding pyroCb initiation, PFT, and the F/U ratio; satellite imagery of the pyroCb; and a time-averaged maximum reflectivity cross-section of the plume will be presented.

4.4.1 10 July

Table 2 Maximum FRP_{x10} from the hour preceding pyroCb initiation, PFT at time of initiation, and F/U ratio for the 10 July pyroCb.

FRP_{x10} [GW]	PFT [GW]	F/U Ratio
1,310	659	~12

The pyroCb on 10 July was a short-lived “puff” which formed over the northwest portion of the Bootleg Fire, initiating at ~22:00 UTC (Fig. 12a). It produced a cold anvil

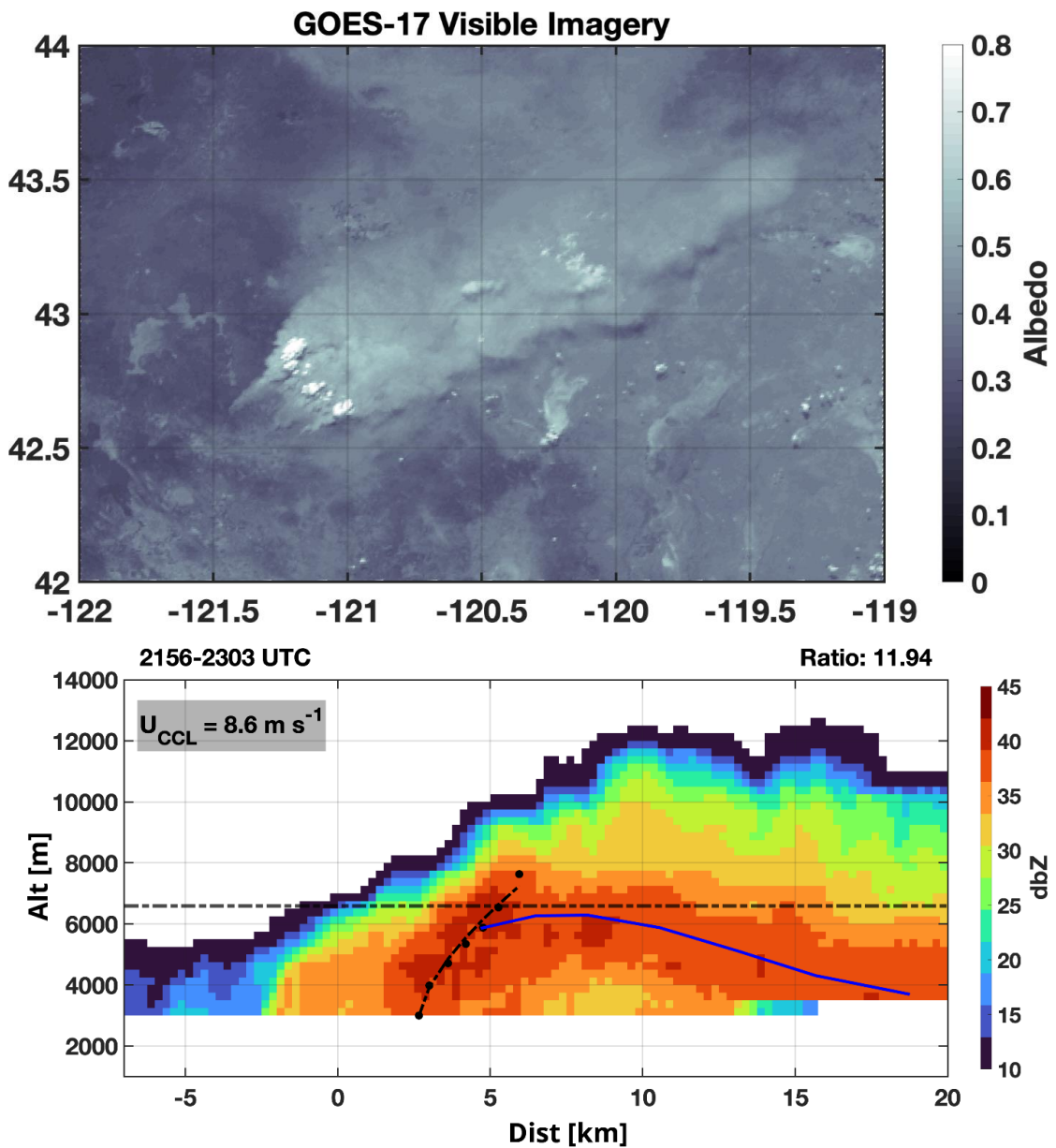


Figure 12 (a) PyroCb pulse over the Bootleg Fire on 10 July at 22:17 UTC seen on GOES-17 visible “red” imagery, and (b) radar cross-section with maximum radar reflectivity from 21:56 through 23:03 UTC on 14 July with Briggs’ plume rise curves overlaid, and corresponding mixed layer winds speeds and F/U ratios.

which quickly detached from the updraft and detrained downwind over the ensuing hour.

Fig. 12b depicts the along-wind maximum radar reflectivity cross-section with the CCL height (6,591 m), average mixed layer wind speed (8.6 m/s), manually selected updraft

core center points (black dots), the Briggs' plume rise curve fit to the centerline points (black dashed line), and the downwind continuation of the plume core (blue line) overlaid on top.

According to Table 2, the FRP_{x10} on this day was about twice the PFT (or 651 GW more), which is amongst the largest P_{diff} values during our observation period (refer to Figs. 5b and 10). Despite the large exceedance, the fire produced only a short-lived pyroCb “puff.” This low-end pyroCb behavior makes more sense when we examine the F/U ratio, which was ~ 12 (unitless), and (as we will show) is small compared to other pyroCb-producing scenarios from the Bootleg Fire. Thus, in this case there is a relatively low “power of the fire versus power of the wind,” which is visually apparent in Fig. 12b’s strongly bent-over smoke plume with an updraft core that approaches the CCL at a small angle. This is an idea we will continue to consider as we observe another pyroCb-producing environment from the Bootleg Fire.

4.4.2 14 July

Table 3 Maximum FRP_{x10} from the hour preceding pyroCb initiation, PFT at time of initiation, and F/U ratio for the 14 July pyroCb.

FRP_{x10} [GW]	PFT [GW]	F/U Ratio
910	379	~ 19.25

We contrast the 10 July pyroCb “puff” to 14 July, which saw a long-lived pyroCb initiate on the southernmost portion of the Bootleg Fire at $\sim 22:30$ UTC (Fig. 13a) and

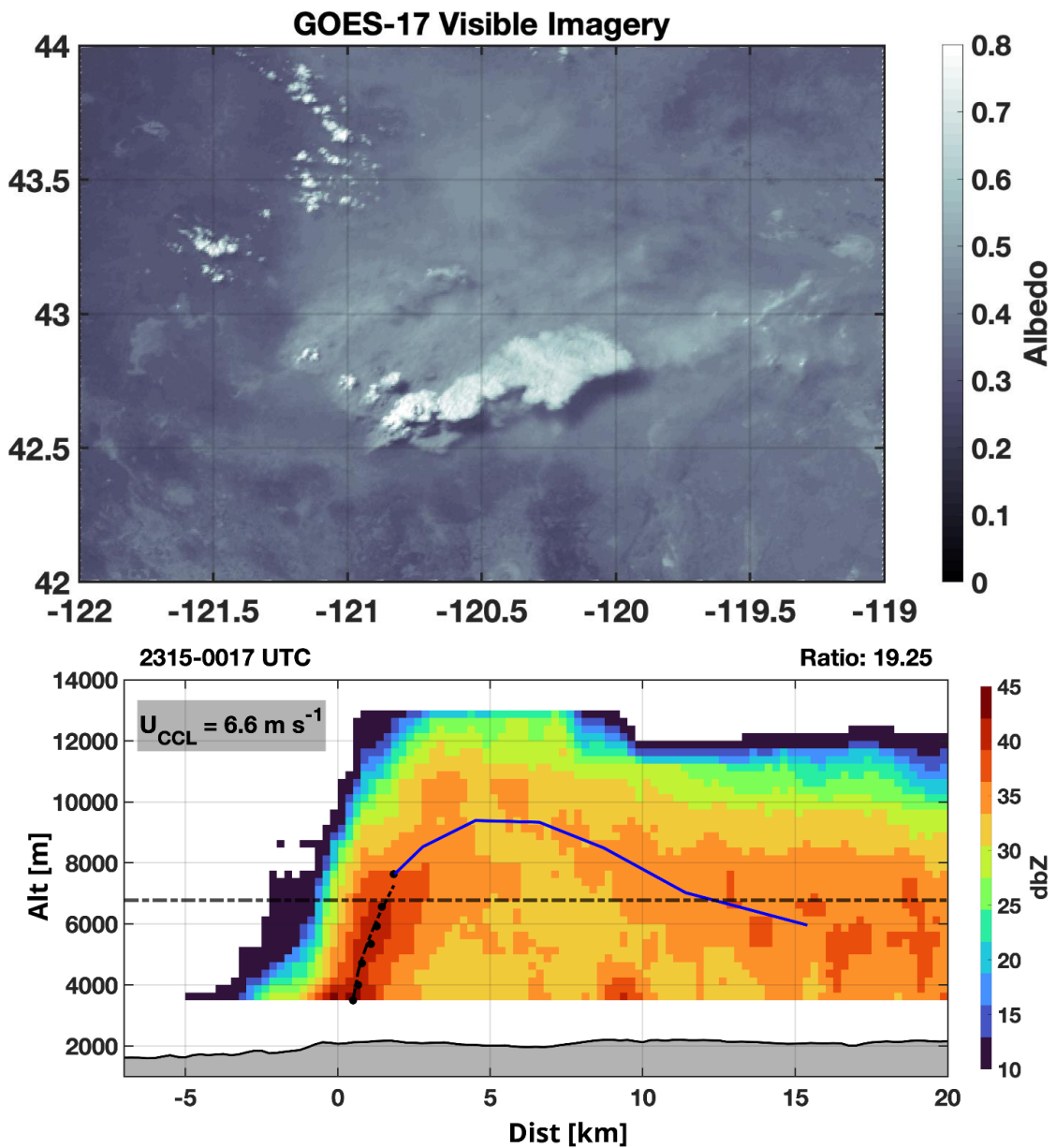


Figure 13 (a) PyroCb pulse over the Bootleg Fire on 14 July at 23:32 UTC seen on GOES-17 visible “red” imagery, and (b) radar cross-section with maximum radar reflectivity from 23:10 UTC on 14 July through 00:12 UTC on 15 July with Briggs’ plume rise curves overlaid, and corresponding mixed layer winds speeds and F/U ratios.

persisting well beyond sunset to ~03:45 on 15 July (see also Fig. 5). Fig. 12b an upright high reflectivity plume core that approaches the CCL at a steep angle and extends further aloft than on 10 July. Table 3 details an environment with an $\text{FRP}_{\times 10}$ of 910 GW, which is

~2.4 times the PFT. The 14 July F/U ratio is larger (19.25) than on 10 July due in part to the decrease in mixed-layer winds (6.6 m/s on 14 July compared to 8.6 m/s on 10 July). Thus, despite the weaker fire, the plume is more upright and the pyroCb more sustained due to larger mass flux crossing the CCL and feeding the cloud.

Future work should explore the plume rise geometry of pyroCb producing plumes in more depth and across a wider range of cases. The results may add to our ability to discriminate amongst pyroCb behaviors and infer variations in fire intensity from plume properties (e.g., more bent-over versus more upright).

5. Discussion and Conclusions

This study of the Bootleg Fire elucidates the fire and atmospheric controls on the initiation and development of pyroCu/Cb. The recurrent day-to-day variations in plume depth and cloud development make this fire an ideal testbed for pyroCu/Cb forecasting approaches.

The first component of our analysis indicates that the condensation level of the Bootleg Fire's plume is well-approximated by the ambient convective condensation level (CCL). Specifically, when the radar-detected plume tops exceed the CCL (i.e., ΔH is positive) pyroCu pixel detections commence. PyroCu subsequently become more prevalent with increasing plume depth above the CCL, and pyroCb typically commence for ΔH of ~1000 m. In contrast, pyroCu/Cb pixels occurrences do not correspond to the plume crossing the LCL. These findings are consistent with previous work indicating the appropriateness of the CCL for forecasting pyroCu/Cb (Lareau and Clements 2016). This

finding also suggests that the CCL can be used as an approximation for more exact expressions for a plume's condensation level used in some pyroCb forecasts tools (e.g., Tory and Kepert, 2021).

The second component of our analysis examined the role of Fire CAPE and Fire CIN in modulating the likelihood of pyroCb. From this analysis, two “end-member” pathways towards pyroCb formation are apparent. First, environments characterized by high-Fire CAPE and low-Fire CIN (deemed High-Low) were found on many days with pyroCb. On these days, relatively small fire heating (i.e., FRP_{x10}) is adequate for overcoming the minimal convective inhibition and plumes that condense can access more instability aloft. Second, pyroCb can form in environments characterized by low-Fire CAPE and high-Fire CIN (Low-High) as well. Here, relatively large convective inhibition below the CCL must be overcome and there is less, or even no, moist instability available if a plume condenses. While this scenario is less conducive to pyroCb at a first glance, we find days where the fire heating is sufficiently large may overcome the Fire CIN and force deep convective development, which is likely largely fed by strong subcloud updrafts. These plumes are thus driven more by firepower rather than moist instability. Between these extremes a range of conditions can yield pyroCb. This analysis emphasizes the need to consider the fire's intensity in the context of the environmental thermodynamics rather than simply assessing the environment.

Third, we tested an explicit approach at quantifying when pyroCb will form, namely the PyroCb Fire-power Threshold (PFT, Tory and Kepert 2021). Indeed, when FRP_{x10} exceeds the PFT, pyroCb were observed in most cases. In that the PFT can be

defined from operational weather forecast models and the FRP can be measured by operational satellites (e.g., GOES), the PFT approach appears to offer a clear path forward for now-casting pyroCb. To this end, we also tested a simple approximation for the PFT (PFT_{approx}), finding equally good results.

Finally, we inspected the impact of plume-rise steepness on pyroCb characteristics. Here we use the plume uprightness as a measure of the power of the fire relative to the power of the wind, as expressed by the F/U ratio. Radar cross-sections through pyroCb plume cores revealed that in a few cases the deeper, colder pyroCb were linked to more upright plumes with plume cores extending far beyond the CCL. In contrast, cases where the plume core was more bent-over produced more tenuous pyroCb. Future work should more broadly examine the plume structure as a controlling factor in pyroCb evolution.

We conclude by noting that this case study of the Bootleg Fire's pyroconvection is amongst only a handful of studies to examine pyroCu/Cb plume rise and cloud initiation processes in detail. Our results help establish a better understanding of our ability to predict when and where pyroCb will occur as well as improving our now-casting capabilities of plume rise outcomes. One clear direction for future work is better quantification of fire power and fire heat fluxes, including how they vary spatially within a fire. Current satellite observations are too coarse for this sort of analysis, but field observations may provide new insights into the process chain controlling pyroconvection and its feedback on the fire.

References

- Alaska Incident Management Team, 2021: 2021 Bootleg Fire Executive Summary July 27-August 5, 2021. Bureau of Land Management. Accessed 3 September 2024, https://fire.ak.blm.gov/content/aicc/team_left/03.%20Alaska%20CIMT%20Incident%20Archive/Alaska%20IMT%20Incident%20Summaries/2021%20Summaries/2021%2007-23%20to%2008-06%20Bootleg.pdf.
- American Meteorological Society, 2021: “Pyrocumulonimbus”. Glossary of Meteorology, <https://glossary.ametsoc.org/wiki/Pyrocumulonimbus>.
- Barry, K.R., and Coauthors, 2021: Observations of Ice Nucleating Particles in the Free Troposphere From Western US Wildfires. *J. Geophys. Res. Atmos.*, 126(3), e2020JD033752, <https://doi.org/10.1029/2020JD033752>.
- Briggs, G.A., 1975: Plume rise predictions. *Lectures on Air Pollution and Environmental Impact Analysis*, 59-111.
- Byram, G.M., 1959: Combustion of forest fuels. *Forest Fire Control and Use*, McGraw-Hill Book Company, 61-89.
- Clark, T.L., Jenkins, M.A., Coen, J., and Packham, D., 1996a: A coupled atmosphere-fire model: Convective feedback on fire-Line dynamics. *J. Appl. Meteor. Climatol.*, 35(6), 875-901, [https://doi.org/10.1175/1520-0450\(1996\)035<0875:ACAMCF>2.0.CO;2](https://doi.org/10.1175/1520-0450(1996)035<0875:ACAMCF>2.0.CO;2).
- Clark, T.L., Jenkins, M.A., Coen, J.L., and Packham, D., 1996b: A coupled atmosphere-fire model: Role of the convective froude number and dynamic fingering at the fireline. *International Journal of Wildland Fire*, 6(4), 177-190, <https://doi.org/10.1071/WF9960177>.
- Dennison, P.E., Brewer, S.C., Arnold, J.D., and Moritz, M.A., 2014: Large wildfire trends in the western United States, 1984-2011. *Geo. Phys. Lett.*, 41(8), 2928-2933, <https://doi.org/10.1002/2014GL059576>.
- Doswell III, C.A., and Rasmussen, E.N., 1994: The Effect of Neglecting the Virtual Temperature Correction on CAPE Calculations. *Wea. Forecasting*, 9(4), 625-629, [https://doi.org/10.1175/1520-0434\(1994\)009<0625:TEONTV>2.0.CO;2](https://doi.org/10.1175/1520-0434(1994)009<0625:TEONTV>2.0.CO;2)
- Dowdy, A.J., Fromm, M.D., and McCarthy, N., 2017: Pyrocumulonimbus lightning and fire ignition on Black Saturday in southeast Australia. *JGR Atmospheres*, 122(14), 7342-7354, <https://doi.org/10.1002/2017JD026577>.
- Dowdy, A.J., Ye, H., Pepler, A., Thatcher, M., Osbrough, S.L., Evans, J.P., Di Virgilio, G., and McCarthy, N., 2019: Future changes in extreme weather and

- pyroconvection risk factors for Australian wildfires. *Scientific Reports*, 9, <https://doi.org/10.1038/s41598-019-46362-x>.
- Dowell, D. C., and Coauthors, 2022: The High-Resolution Rapid Refresh (HRRR): An hourly updating convection-allowing forecast model. Part I: Motivation and system description. *Wea. Forecasting*, 37(8), 1371–1395, <https://doi.org/10.1175/WAF-D-21-0151.1>.
- Eghdami, M., Juliano, T.W., Jiménez, P.A., Kosovic, B., Castellnou, M., Kumar, R., and Vila-Guerau de Arellano, J., 2023: Characterizing the Role of Moisture and Smoke on the 2021 Santa Coloma de Queralt Pyroconvective Event Using WRF-Fire. *J. Adv. Model. Earth Syst.*, 15(5), e2022MS003288, <https://doi.org/10.1029/2022MS003288>.
- Fromm, M., Servranckx, R., Stocks, B.J., and Peterson, D.A., 2022: Understanding the critical elements of the pyrocumulonimbus storm sparked by high-intensity wildland fire. *Nature*, 3, <https://doi.org/10.1038/s43247-022-00566-8>.
- Fromm, M., Tupper, A., Rosenfeld, D., Servranckx, R., and McRae, R., 2006: Violent pyro-convective storm devastates Australia's capital and pollutes the stratosphere. *Geophys. Res. Lett.*, 33(5), <https://doi.org/10.1029/2005GL025161>.
- Haines, D.A., 1988: A lower atmospheric severity index for wildland fires. *National Weather Digest*, 13, 23-27.
- Juliano, T.W., and Coauthors, 2023: Toward a Better Understanding of Wildfire Behavior, in the Wildland-Urban Interface: A Case Study of the 2021 Marshall Fire. *Geo. Res. Lett.*, 50(10), e2022GL101557, <https://doi.org/10.1029/2022GL101557>.
- Juliano, T.W., Szasdi-Bardales, F., Lareau, N.P., Shamsaei, K., Kosović, B., Elhami-Khorasani, N., James, E.P., and Ebrahimian, H., 2024: Brief communication: The Lahaina Fire disaster – how models can be used to understand and predict wildfires. *Natural Hazards and Earth System Sciences*, 24(1), 47-52, <https://doi.org/10.5194/nhess-24-47-2024>.
- Lareau, N.P., and Clements, C.B., 2016: Environmental controls on pyrocumulus and pyrocumulonimbus initiation and development. *Atmos. Chem. Phys.*, 16(6), 4005-4022, <https://doi.org/10.5194/acp-16-4005-2016>.
- Lareau, N.P., and Clements, C.B., 2017: The Mean and Turbulent Properties of a Wildfire Convective Plume. *J. Appl. Meteor. Climatol.*, 56(8), 2289-2299, <https://doi.org/10.1175/JAMC-D-16-0384.1>.

- Lareau, N.P., Nauslar, N.J., and Abatzoglou, J.T., 2018: Carr Fire Vortex: A Case of Pyrotornadogenesis? *Geo. Phys. Lett.*, 45(23), 13107-13115, <https://doi.org/10.1029/2018GL080667>.
- Lareau, N.P., Nauslar, N.J., Bentley, E., Roberts, M., Emmerson, S., Bronge, B., Mehlef, M., and Wallman, J., 2022: Fire-Generated Tornadic Vortices. *Bull. Amer. Meteor. Soc.*, 103(5), E1296–E1320, <https://doi.org/10.1175/BAMS-D-21-0199.1>.
- Leach, R.N., and Gibson, C.V., 2021: Assessing the Potential for Pyroconvection and Wildfire Blow Ups. *J. Operational Meteor.*, 9(4), 47-61, <https://doi.org/10.15191/nwajom.2021.0904>.
- Liu, C.-C., Portmann, R. W., Liu, S., Rosenlof, K. H., Peng, Y., and Yu, P., 2022: Significant effective radiative forcing of stratospheric wildfire smoke. *Geophysical Research Letters*, 49(17), e2022GL100175, <https://doi.org/10.1029/2022GL100175>.
- Luderer, G., Trentmann, J., and Andreae, M.O., 2009: A new look at the role of fire-released moisture on the dynamics of atmospheric pyro-convection. *International Journal of Wildland Fire*, 18(5), 554-562, <https://doi.org/10.1071/WF07035>.
- McCarthy, N., Guyot, A., Dowdy, A., and McGowan, H., 2019: Wildfire and Weather Radar: A Review. *Journal of Geophysical Research: Atmospheres*, 124(1), 266-286, <https://doi.org/10.1029/2018JD029285>.
- McCluskey, C.S., and Coauthors, 2014: Characteristics of atmospheric ice nucleating particles associated with biomass burning in the US: Prescribed burns and wildfires. *J. Geophys. Res. Atmos.*, 119(17), 10,458-10,470, <https://doi.org/10.1002/2014JD021980>.
- Mills, G.A., and McCaw, L., 2010: Atmospheric Stability Environments and Fire Weather in Australia – extending the Haines index. *CAWCR Technical Report No. 20*, 151 pp., http://cawcr.gov.au/technical-reports/CTR_020.pdf.
- Morvan, D. and Frangieh, N., 2017: Wildland fires behaviour: wind effect versus Byram's convective number and consequences upon the regime of propagation. *International Journal of Wildland Fire*, 27(9), 636-641.
- Nauslar, N.J., Abatzoglou, J.T., and Marsh, P.T., 2018: The 2017 North Bay and Southern California Fires: A Case Study. *Fire*, 1(1), 18, <https://doi.org/10.3390/fire1010018>.
- Peterson, D. A., Campbell, J. R., Hyer, E. J., Fromm, M. D., Kablick III, G. P., Cossuth, J. H., and DeLand, M. T., 2018: Wildfire-driven thunderstorms cause a volcano-

- like stratospheric injection of smoke. *NPJ climate and atmospheric science*, 1, <https://doi.org/10.1038/s41612-018-0039-3>.
- Peterson, D. A., Fromm, M. D., McRae, R. H., Campbell, J. R., Hyer, E. J., Taha, G., ... and DeLand, M. T., 2021: Australia's Black Summer pyrocumulonimbus super outbreak reveals potential for increasingly extreme stratospheric smoke events. *NPJ climate and atmospheric science*, 4, <https://doi.org/10.1038/s41612-021-00192-9>.
- Peterson, D.A., Fromm, M.D., Solbrig, J.E., Hyer, E.J., Surratt, M.L., and Campbell, J.R., 2017a: Detection and Inventory of Intense Pyroconvection in Western North America using GOES-15 Daytime Infrared Data. *J. Appl. Meteor. Climatol.*, 56(2), 471-493, <https://doi.org/10.1175/JAMC-D-16-0226.1>.
- Peterson, D.A., Hyer, E.J., Campbell, J.R., Fromm, M.D., Hair, J.W., Butler, C.F., and Fenn, M.A., 2015: The 2013 Rim Fire: Implications for Predicting Extreme Fire Spread, Pyroconvection, and Smoke Emissions. *Bull. Am. Meteorol.*, 96(2), 229-247, <https://doi.org/10.1175/BAMS-D-14-00060.1>.
- Peterson, D.A., Hyer, E.J., Campbell, J.R., Solbrig, J.E., and Fromm, M.D., 2017b: A Conceptual Model for Development of Intense Pyrocumulonimbus in Western North America. *Monthly Weather Review*, 145(6), 2235-2255, <https://doi.org/10.1175/MWR-D-16-0232.1>.
- Potter, B.E., 2012: Atmospheric interactions with wildland fire behaviour – II. Plume and vortex dynamics, *International Journal of Wildland Fire*. 21(7), 802-817, <https://doi.org/10.1071/WF11129>.
- Potter, B.E., 2018: The Haines Index – it's time to revise it or replace it. *International Journal of Wildland Fire*. 27(7), 437-440, <https://doi.org/10.1071/WF18015>.
- Potter, B.E., and Anaya, M.A., 2015: A Wildfire-relevant climatology of the convective environment of the United States. *International Journal of Wildland Fire*. 24, 267-275, <https://doi.org/10.1071/WF13211>.
- Rodriguez, B., Lareau, N.P., Kingsmill, D.E., and Clements, C.B., 2020: Extreme Pyroconvective Updrafts During a Megafire. *Geophysical Research Letters*. 47(18), <https://doi.org/10.1029/2020GL089001>.
- Schmidt, C.C., Hoffman, J., Prins, E., Lindstrom, S., 2020: GOES-R Advanced Baseline Imager (ABI) Algorithm Theoretical Basis Document For Fire/Hot Spot Characterization. NOAA NESDIS Center for Satellite Applications and Research.

- Sullivan, A.L., 2007: Convective Froude number and Byram's energy criterion of Australian experimental grassland fires. *Proceedings of the Combustion Institute*, 31(2), 2557-2564, <https://doi.org/10.1016/j.proci.2006.07.053>.
- Tory, K. J., 2019: Pyrocumulonimbus firepower threshold: A pyrocumulonimbus prediction tool. *Australian Journal of Emergency Management Monograph No. 5*, December 2019, pp 21—27. Extended abstracts from the Bushfire and Natural Hazards Cooperative Research Centre Research Forum. <https://www.aidr.org.au/media/7379/monograph-no5-extended-abstracts-final.pdf>.
- Tory, K.J., and Kepert, J.D., 2021: Pyrocumulonimbus Firepower Threshold: Assessing the Atmospheric Potential for pyroCb. *Wea. Forecasting*, 36(2), 439-456, <https://doi.org/10.1175/WAF-D-20-0027.1>.
- Tory, K.J., Thurston, W., and Kepert, J.D., 2018: Thermodynamics of Pyrocumululus: A Conceptual Study. *Mon. Wea. Rev.*, 146(8), 2579-2598, <https://doi.org/10.1175/MWR-D-17-0377.1>.
- Trentmann, J., and Coauthors, 2006: Modeling of biomass smoke injection into the lower stratosphere by a large forest fire (Part I): reference simulation. *Atmospheric Chemistry and Physics*, 6(12), 5247-5260, <https://doi.org/10.5194/acp-6-5247-2006>.
- Thurston, W., Tory, K.J., Fawcett, R.J.B., and Kepert, J.D., 2015: Large-eddy simulations of pyro-convection and its sensitivity to environmental conditions. *Proc. 20th Int. Congress on Modelling and Simulation*, Adelaide, South Australia, Australia, Modeling and Simulation Society of Australia and New Zealand, 284-289.
- Val Martin, M., Kahn, R.A., Logan, J.A., Paugam, R., Wooster, M., and Ichoku, C., 2012: Space-based observational constraints for 1-D fire smoke plume-rise models. *J. Geophys. Res. Atmos.*, 117(D22), <https://doi.org/10.1029/2012JD018370>.
- Westerling, A.L., 2016: Increasing western US forest wildfire activity: sensitivity to changes in the timing of spring. *Philosophical Transactions of the Royal Society B*, 371(1696), <https://doi.org/10.1098/rstb.2015.0178>.
- Westerling, A.L., Hidalgo, H.G., Cayan, D.R., and Swetnam, T.W., 2006: Warming and Earlier Spring Increase Western U.S. Forest Wildfire Activity. *Science*, 313(5789), 940-943, <https://doi.org/10.1126/science.1128834>.
- Wilmot, T.Y., Mallia, D.V., Hallar, A.G., and Lin, J.C., 2022: Wildfire plumes in the Western US are reaching greater heights and injecting more aerosols aloft as

wildfire activity intensifies. *Sci. Rep.*, 12, <https://doi.org/10.1038/s41598-022-16607-3>.

Winkler, J.A., Potter, B.E., Wilhelm, D.F., Shadbolt, R.P., Piromsopa, K., and Bian, X., 2007: Climatological and statistical characteristics of the Haines Index for North America. *International Journal of Wildland Fire*, 16,139-152.

Wotten, B.M., Flannigan, M.D., and Marshall, G.A., 2017: Potential climate change impacts on fire intensity and key wildfire suppression thresholds in Canada. *Environ. Res. Lett.*, 12(9), <https://doi.org/10.1088/1748-9326/aa7e6e>.